


 Cite this: *Chem. Commun.*, 2020, 56, 15639

 Received 24th March 2020,  
Accepted 19th November 2020

DOI: 10.1039/d0cc02150d

rsc.li/chemcomm

## p–p orbital interaction *via* magnesium isovalent doping enhances optoelectronic properties of halide perovskites†

 Feng Qian,<sup>†a</sup> Jue Gong,<sup>†b</sup> Mingyu Hu,<sup>ab</sup> Chunyu Ge,<sup>†a</sup>  
Nitin P. Padture,<sup>†b</sup> Yuanyuan Zhou<sup>†\*bc</sup> and Jing Feng<sup>\*a</sup>

**p–p orbital interaction through Mg(II) isovalent doping in methylammonium lead chloride perovskite significantly enhances the electronic properties while not affecting the optical bandgap. This chemical behaviour shows promising applications to optoelectronic devices.**

Owing to the suitable optical bandgap of 2.9 eV, methylammonium lead trichloride (CH<sub>3</sub>NH<sub>3</sub>PbCl<sub>3</sub> or MAPbCl<sub>3</sub>) perovskite is potentially useful in various applications such as deep-color light-emitting diodes, lasers, transparent photovoltaics, and ultraviolet (UV) photodetectors.<sup>1–6</sup> However, the high electronegativity of Cl<sup>–</sup> can have an adverse effect on carrier mobilities of this perovskite material,<sup>7</sup> resulting in poor electronic properties and limiting the device performance. For mitigating this issue, composition engineering approaches may be used, which entail the replacement of either MA<sup>+</sup> or Cl<sup>–</sup> with alternative ions.<sup>8–13</sup> But such practices inevitably bring about changes in the key optical bandgap of MAPbCl<sub>3</sub>. For improving the electronic properties, while maintaining the wide-bandgap nature, one can only resort to substitution of the B-site cations (Pb<sup>2+</sup>) in MAPbCl<sub>3</sub>. As a group IIA element, Mg<sup>2+</sup> has a different valence electron configuration (2s<sup>2</sup>2p<sup>6</sup>) from Pb<sup>2+</sup> (6s<sup>2</sup>). As shown in Fig. 1a, when forming chemical bonds with Cl<sup>–</sup> (3s<sup>2</sup>3p<sup>6</sup>), the p–p orbital interaction between Mg<sup>2+</sup> and Cl<sup>–</sup> is expected to give rise to more polarizable electrons and thus higher carrier mobilities in materials because of greater spatial orbital overlap, as compared with the s–p interaction between Pb<sup>2+</sup> and Cl<sup>–</sup> shown in Fig. 1b. Furthermore, due to relativistic effects, Pb 6s orbitals are stabilized through spatial contraction,<sup>14</sup> which will additionally

cause the bonding electrons in Pb–Cl network to be less mobile. In addition, in contrast to that for the 6s<sup>2</sup> electrons of Pb<sup>2+</sup>, the density distribution for the 2p<sup>6</sup> electrons of Mg<sup>2+</sup> are in much closer proximity to the nucleus, contributing to tighter chemical bonding between Mg<sup>2+</sup> and Cl<sup>–</sup>, and thus, higher chemical stability of the perovskite.<sup>15</sup> As such, herein we demonstrate Mg-doping (Fig. 1c) as a promising strategy for improving the electronic properties of MAPbCl<sub>3</sub> while maintaining its bandgap. Based on this approach, UV photodetectors with enhanced performance and stability are successfully fabricated.

In order to confirm the Mg-doping mechanism in MAPbCl<sub>3</sub>, we first synthesized Mg-doped MAPbCl<sub>3</sub> (denoted as Mg:MAPbCl<sub>3</sub>) single-crystals using the antisolvent-vapor-assisted crystallization method.<sup>16</sup> Here, PbCl<sub>2</sub>, MAcl, and MgCl<sub>2</sub> are co-dissolved in dimethyl sulfoxide in molar ratios of 1:1:0.15 to form the precursor solution. Note that the atomic ratios in the precursor solution do not necessarily represent the composition of the final product. Subsequently, the solution was placed in an atmosphere of dichloromethane antisolvent vapor at room temperature, where

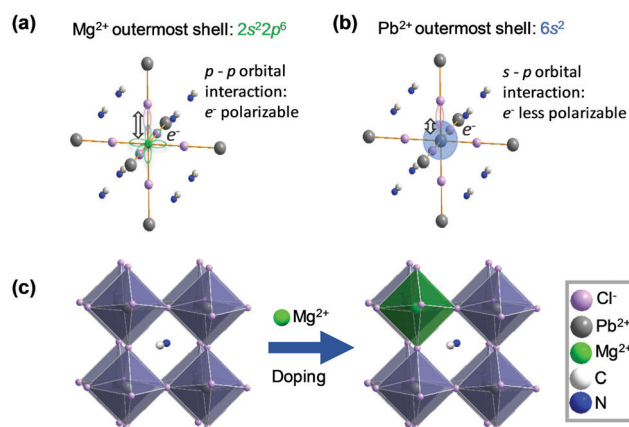


**Fig. 1** (a) Schematic illustrations of orbital interactions in (a) Mg–Cl and (b) Pb–Cl bonds. (c) Schematic illustration of Mg-doping in MAPbCl<sub>3</sub> via cation substitution.

<sup>a</sup> Faculty of Materials Science and Engineering, Kunming University of Science and Technology, Kunming, Yunnan 650093, China. E-mail: jingfeng@kmust.edu.cn

<sup>b</sup> School of Engineering, Brown University, Providence, Rhode Island, 02912, USA. E-mail: nitin\_padture@brown.edu

<sup>c</sup> Department of Physics, Hong Kong Baptist University (HKBU), Hong Kong SAR, China. E-mail: yzzhou@hkbu.edu.hk

† Electronic supplementary information (ESI) available. See DOI: 10.1039/d0cc02150d

‡ These authors contributed equally.

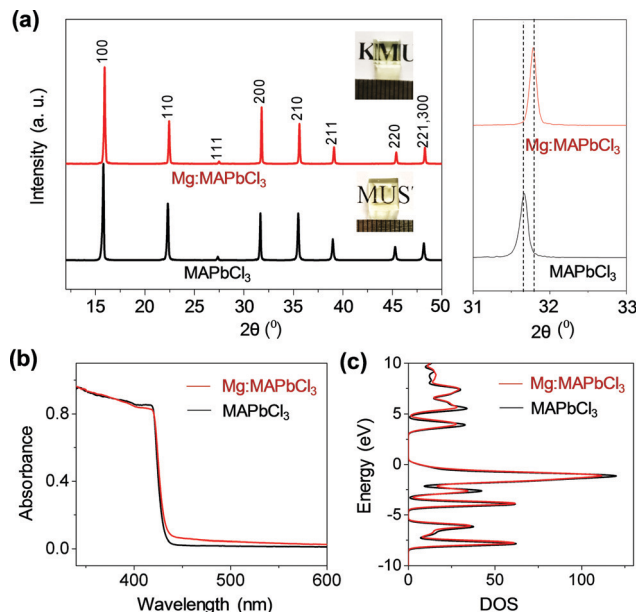


Fig. 2 (a) XRD patterns of Mg:MAPbCl<sub>3</sub> and pure MAPbCl<sub>3</sub> samples prepared by grinding the single-crystals into fine powders. Insets are the photographs of the original single-crystals. (b) UV-vis absorption spectra of Mg:MAPbCl<sub>3</sub> and pure MAPbCl<sub>3</sub> single-crystals. (c) Calculated DOS of Mg:MAPbCl<sub>3</sub> and pure MAPbCl<sub>3</sub>.

the Mg:MAPbCl<sub>3</sub> single-crystals grow slowly. Pure MAPbCl<sub>3</sub> single-crystals were also grown without the addition of MgCl<sub>2</sub>. A more detailed experimental synthesis procedure is included in the ESI.† Fig. 2a compares the powder X-ray diffraction (XRD) patterns of ground samples of pure MAPbCl<sub>3</sub> and Mg:MAPbCl<sub>3</sub> single-crystals (inset shows photographs). Both samples show well-resolved XRD peaks that can be fully indexed based on the cubic *Pm* $\bar{3}$ *m* symmetry. Importantly, the characteristic (200) peak for Mg:MAPbCl<sub>3</sub> shifts to higher  $2\theta$  compared with that for pure MAPbCl<sub>3</sub>, confirming a decrease of the lattice parameter (from  $a = 0.564$  nm to  $a = 0.562$  nm) of the cubic perovskite crystal structure. This suggests that  $\sim 2$  at% of Pb<sup>2+</sup> (ionic radius: 119 pm) ions are substituted by Mg<sup>2+</sup> (ionic radius: 72 pm) in the crystal structure according to the Vegard's law.<sup>17,18</sup> We also studied the effect of Mg-doping content on the phase and structure of Mg:MAPbCl<sub>3</sub> single-crystals. As shown in Fig. S1 (ESI†), when the amount of Mg<sup>2+</sup> precursors (MgCl<sub>2</sub>) in the solution is increased, the lattice parameter is further reduced, indicating incorporation of more Mg<sup>2+</sup> in the crystal structure. However, impurity phases are also identified in the resulting crystals with higher Mg-doping content, which can be attributed to phase segregation. In general, we do not observe a noticeable effect of Mg-doping on the macroscopic shape of the as-grown MAPbCl<sub>3</sub>, which is mostly related to the low doping level. The UV-vis absorption spectra of Mg:MAPbCl<sub>3</sub> and pure MAPbCl<sub>3</sub> are compared in Fig. 2b, exhibiting the same band edge at  $\sim 430$  nm. The corresponding Tauc plots in Fig. S2 (ESI†) reveal the same bandgap, 2.90 eV, in both Mg:MAPbCl<sub>3</sub> and pure MAPbCl<sub>3</sub> single-crystals. We further calculated density of states (DOS) for Mg:MAPbCl<sub>3</sub> and pure MAPbCl<sub>3</sub> as shown in Fig. 2c, which again reveals the same bandgap for Mg:MAPbCl<sub>3</sub> and pure MAPbCl<sub>3</sub>.

This is because there are negligible effects of *s* or *p* orbitals of Mg on the Pb or Cl orbital energy levels near the bandgap (see Fig. S3, ESI,† for more details).

X-ray photoelectron spectroscopy (XPS) studies were conducted to elucidate the effects of Mg-doping on the chemical bonding in the perovskite structure. As shown in Fig. 3a, XPS survey scans confirm the existence of Pb, Cl, and C elements in both Mg:MAPbCl<sub>3</sub> and pure MAPbCl<sub>3</sub> single-crystal samples. By scrutinizing the binding energy region between 200 and 400 eV, we observed an intensity peak at  $\sim 300$  eV that can be attributed to Mg KLL Auger photoelectrons<sup>19</sup> (Fig. 3b), which attests the existence of Mg in Mg:MAPbCl<sub>3</sub>. Furthermore, XPS resolution scans in Fig. 3c reveal a larger binding energy of Cl 2p electrons in Mg:MAPbCl<sub>3</sub> than that in pure MAPbCl<sub>3</sub>, which indicates that the conceptualized p-p orbital interaction brings forth a tight bonding in the Mg-Cl network. Meanwhile, we observed smaller binding energy of Pb 4f electrons in Mg:MAPbCl<sub>3</sub> (Fig. 3d), which is consistent with moderate Pb-Cl connection by Mg-doping. Also, Cl 2p electrons show a much smaller binding-energy difference (0.04 eV) between Mg:MAPbCl<sub>3</sub> and MAPbCl<sub>3</sub> than Pb 4f electrons, which is attributed to the more polarizable p-p electrons in Mg-Cl bonds than the electrons in Pb-Cl bonds.

Lateral photoconductor-type electron-only devices (see Fig. S4, ESI,† for the dimensions of interdigitated gold electrodes) based on Mg:MAPbCl<sub>3</sub> and pure MAPbCl<sub>3</sub> single-crystals were fabricated for understanding the effect of Mg-doping on the electronic properties. Under dark conditions, space-charge-limited current (SCLC) measurements reveal a much lower trap-filled limit voltage ( $V_{\text{TFL}}$ ) for Mg:MAPbCl<sub>3</sub> (0.337 V, Fig. 4b) with respect to MAPbCl<sub>3</sub> single-crystal (1.460 V, Fig. 4a). Correspondingly the trap density ( $n_{\text{Trap}}$ ) of electrons in Mg:MAPbCl<sub>3</sub> is three times lower than that in pure MAPbCl<sub>3</sub> based on the following equation,<sup>20</sup>

$$n_{\text{traps}} = \frac{2\epsilon_r\epsilon_0 V_{\text{TFL}}}{qd^2}, \quad (1)$$

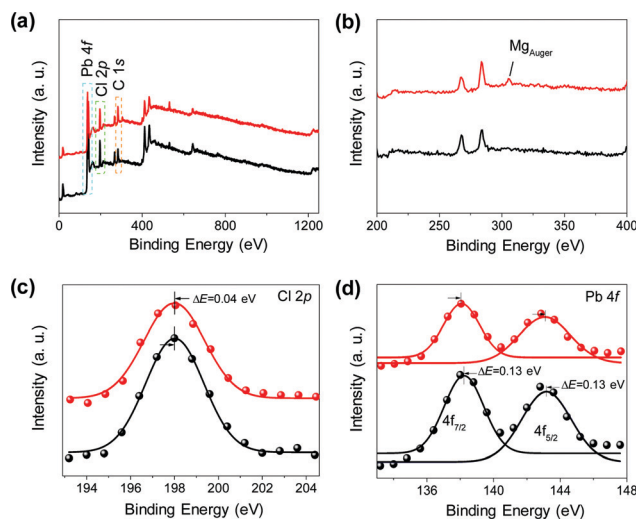


Fig. 3 XPS spectra of Mg:MAPbCl<sub>3</sub> (red) and pure MAPbCl<sub>3</sub> (black) single-crystals: (a) survey scans and (b) zoomed-in view of survey scans. Higher resolution scans of: (c) Cl 2p and (d) Pb 4f electrons.

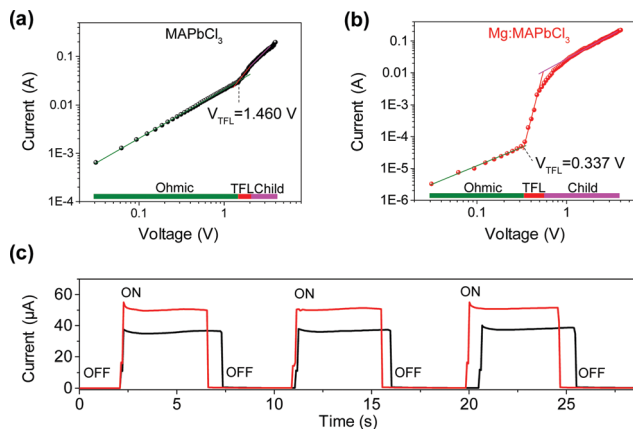


Fig. 4 SCLC plots for single-crystals: (a) pure MAPbCl<sub>3</sub> and (b) Mg:MAPbCl<sub>3</sub>. (c) On-off switching performance under 365 nm UV illumination of photodetectors based on pure MAPbCl<sub>3</sub> (black) and Mg:MAPbCl<sub>3</sub> (red) single-crystals.

where  $\epsilon_r$ ,  $\epsilon_0$ ,  $V_{\text{TFL}}$ ,  $q$ , and  $d$  are the relative permittivity of MAPbCl<sub>3</sub> (23.9),<sup>1,4</sup> vacuum permittivity ( $8.854 \times 10^{-12}$  F m<sup>-1</sup>), trap-filled limit voltage ( $V_{\text{TFL}}$ ), elementary charge, and carrier drift length, respectively. Furthermore, electron mobility of Mg:MAPbCl<sub>3</sub> is determined to be 34% higher than that of pure MAPbCl<sub>3</sub> by fitting the child regimes in Fig. 4a and b using the following equation,<sup>4</sup>

$$J = \frac{9\epsilon_r\epsilon_0\mu V^2}{8d^3} \quad (2)$$

where  $\mu$ ,  $V$ , and  $J$  are carrier mobility, voltage, and current density, respectively. The photocurrent responses of photoconductor devices based on Mg:MAPbCl<sub>3</sub> and pure MAPbCl<sub>3</sub> single-crystals are compared in Fig. 4c. Upon the illumination of 365 nm UV photons with a power density of  $0.0524$  mW cm<sup>-2</sup>, Mg:MAPbCl<sub>3</sub> single-crystal exhibits a photocurrent of  $55$   $\mu$ A, which is much higher than MAPbCl<sub>3</sub> ( $38$   $\mu$ A). This unambiguously confirms the improved optoelectronic device performance due to the Mg-doping.

Vertical thin-film photodetector-type devices are further fabricated by sandwiching the solution-processed halide perovskite layers with n-type and p-type charge extraction layers. The schematic illustrations showing the detailed device structures are included in Fig. S5 (ESI<sup>†</sup>). Near-UV (450 nm) light illumination is used here. Fig. 5a and b show functional responses of photodetector devices based on Mg:MAPbCl<sub>3</sub> and pure MAPbCl<sub>3</sub> thin films, respectively, under varied incident power densities. Fig. 5c plots the photocurrent density as a function of incident power density for the photodetectors based on Fig. 5a and b. It is clear that the Mg:MAPbCl<sub>3</sub>-based photodetector outperforms the MAPbCl<sub>3</sub>-based photodetector, particularly at higher power densities. Fig. 5d compares the magnitude of the photo-response of Mg:MAPbCl<sub>3</sub>-based and pure MAPbCl<sub>3</sub>-based photodetectors. Once again, the Mg:MAPbCl<sub>3</sub>-based photodetector performs significantly better at high power densities ( $>0.13$  W cm<sup>-2</sup>).

Mg-doping also improves the stability of MAPbCl<sub>3</sub> perovskite, which is important for the operation of electronic devices. We monitored the evolution of absorption spectra for Mg:MAPbCl<sub>3</sub> and MAPbCl<sub>3</sub> thin films in a controlled environment (80% relative humidity; 30 °C; air). By tracking the maximum absorbance near

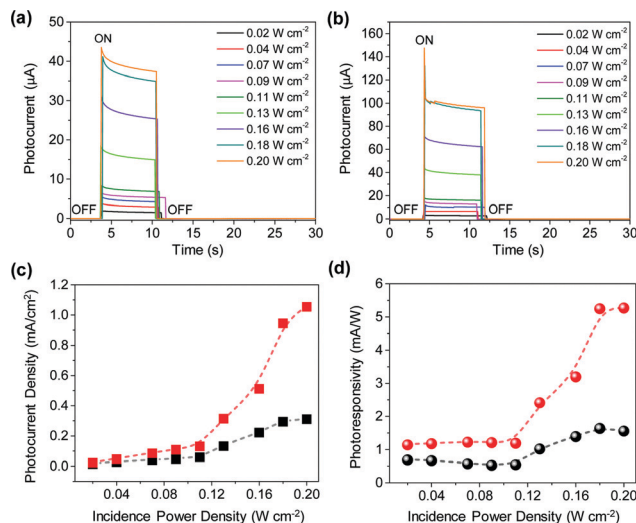


Fig. 5 On-off switching performance under 450 nm light illumination with different incidence power densities of thin-film photodetectors based on: (a) pure MAPbCl<sub>3</sub> and (b) Mg:MAPbCl<sub>3</sub>. Corresponding performance comparisons of the two types of thin-film photodetectors: (c) photocurrent density and (d) photoresponsivity.

400 nm (Fig. S6, ESI<sup>†</sup>), it is evident that the Mg:MAPbCl<sub>3</sub> thin film retains more than 60% of the original absorbance after a period of storage in the ambient air, as compared to only 25% for pure MAPbCl<sub>3</sub>. The storage time is 3 h, which is sufficient for this stability comparison. In terms of device stability (Fig. S7, ESI<sup>†</sup>), the Mg:MAPbCl<sub>3</sub> thin film photodetector has stabilized photocurrents above 90% of the original magnitude during a 25 s continuous output under 450 nm illumination at incident power densities of  $0.02$  W cm<sup>-2</sup> and  $0.09$  W cm<sup>-2</sup>. For comparison, less than 80% of the original currents are retained for the pure MAPbCl<sub>3</sub> device under the same test conditions. The observed material and device photocurrent stabilities corroborate the tighter atomic bonding as imparted by structural analyses mentioned earlier.

In summary, we have demonstrated Mg-doping as an effective method for enhancing electronic properties of MAPbCl<sub>3</sub> perovskites without affecting the critical optical bandgaps, which shows promising applications to high-performance photodetectors. While it is currently challenging to gain more insights into the detailed crystal and defect structures using high-resolution characterizations such as transmission electron microscopy, synchrotron, and spectroscopies primarily due to the soft nature of the as-synthesized perovskite materials,<sup>21</sup> we envision that future research effort in this direction may eventually overcome such characterization obstacles and unveil the exact character of metal doping in perovskites. Finally, this work points to a promising direction in influencing the atomic orbital interaction and chemical bonding through rational metal-doping for halide perovskites with tailored properties.

This research performed at Kunming University of Science and Technology is supported by the National Key R&D Program of China (No. 2019YFB1503200), the National Natural Science Foundation of China (grant No. 11504146 and No. 51762028), and Rare Metal Material Genetic Engineering Project of Yunnan

Province (grant no. 2018ZE019). The research performed at Brown University is supported by the US National Science Foundation (grant No. OIA-1538893).

## Conflicts of interest

There are no conflicts to declare.

## Notes and references

- 1 T. Matsushima, F. Bencheikh, T. Komino, M. R. Leyden, A. S. D. Sandanayaka, C. Qin and C. Adachi, *Nature*, 2019, **572**, 502–506.
- 2 G. Xing, N. Mathews, S. S. Lim, N. Yantara, X. Liu, D. Sabba, M. Gratzel, S. Mhaisalkar and T. C. Sum, *Nat. Mater.*, 2014, **13**, 476–480.
- 3 G. Maculan, A. D. Sheikh, A. L. Abdelhady, M. I. Saidaminov, M. A. Haque, B. Murali, E. Alarousu, O. F. Mohammed, T. Wu and O. M. Bakr, *J. Phys. Chem. Lett.*, 2015, **6**, 3781–3786.
- 4 W. Wang, H. Xu, J. Cai, J. Zhu, C. Ni, F. Hong, Z. Fang, F. Xu, S. Cui, R. Xu, L. Wang, F. Xu and J. Huang, *Opt. Express*, 2016, **24**, 8411–8419.
- 5 E. Zheng, B. Yuh, G. A. Tosado and Q. Yu, *J. Mater. Chem. C*, 2017, **5**, 3796–3806.
- 6 D. Liu, C. Yang and R. R. Lunt, *Joule*, 2018, **2**, 1827–1837.
- 7 J. E. Huheey, E. A. Keiter and R. L. Keiter, *Inorganic Chemistry: Principles of Structure and Reactivity*, HarperCollins College Publishers, New York, 4th edn, 1993.
- 8 Y. Chen, M. He, J. Peng, Y. Sun and Z. Liang, *Adv. Sci.*, 2016, **3**, 1500392.
- 9 J. Gong, X. Li, P. Guo, I. Zhang, W. Huang, K. Lu, Y. Cheng, R. D. Schaller, T. J. Marks and T. Xu, *J. Mater. Chem. A*, 2019, **7**, 13043–13049.
- 10 L. Wang, G. D. Yuan, R. F. Duan, F. Huang, T. B. Wei, Z. Q. Liu, J. X. Wang and J. M. Li, *AIP Adv.*, 2016, **6**, 045115.
- 11 D. Amgar, T. Binyamin, V. Uvarov and L. Etgar, *Nanoscale*, 2018, **10**, 6060–6068.
- 12 S. Draguta, O. Sharia, S. J. Yoon, M. C. Brennan, Y. V. Morozov, J. S. Manser, P. V. Kamat, W. F. Schneider and M. Kuno, *Nat. Commun.*, 2017, **8**, 200.
- 13 W. A. Dunlap-Shohl, Y. Zhou, N. P. Padture and D. B. Mitzi, *Chem. Rev.*, 2019, **119**, 3193–3295.
- 14 J. Autschbach, *J. Chem. Phys.*, 2012, **136**, 150902.
- 15 N. Phung, R. Félix, D. Meggiolaro, A. Al-Ashouri, G. S. e Silva, C. Hartmann, J. Hidalgo, H. Köbler, E. Mosconi, B. Lai, R. Gunder, M. Li, K.-L. Wang, Z.-K. Wang, K. Nie, E. Handick, R. G. Wilks, J. A. Marquez, B. Rech, T. Unold, J.-P. Correa-Baena, S. Albrecht, F. D. Angelis, M. Bär and A. Abate, *J. Am. Chem. Soc.*, 2020, **142**, 2364–2374.
- 16 D. Shi, V. Adinolfi, R. Comin, M. Yuan, E. Alarousu, A. Buin, Y. Chen, S. Hoogland, A. Rothenberger and K. Katsiev, *Science*, 2015, **347**, 519–522.
- 17 R. D. Shannon, *Acta Crystallogr., Sect. A: Cryst. Phys., Diffraction, Theor. Gen. Crystallogr.*, 1976, **32**, 751–767.
- 18 Y. Zhou, Z. Zhou, M. Chen, Y. Zong, J. Huang, S. Pang and N. P. Padture, *J. Mater. Chem. A*, 2016, **4**, 17623–17635.
- 19 A. Talapatra, S. K. Bandyopadhyay, P. Sen, P. Barat, S. Mukherjee and M. Mukherjee, *Phys. C*, 2005, **419**, 141–147.
- 20 R. H. Bube, *J. Appl. Phys.*, 1962, **33**, 1733.
- 21 (a) Y. Zhou, H. Sternlicht and N. P. Padture, *Joule*, 2019, **3**, 641; (b) Y. Zhou, H. Zhou, J. Deng, W. Cho and Z. Cai., *Matter*, 2020, **2**, 360; (c) S. Cai and Y. Zhou, *Joule*, 2020, DOI: 10.1016/j.joule.2020.11.014.